

XSL DR2 (Phase 3 data)

Abstract

We present the second data release (DR2) of the X-Shooter Spectral Library (XSL), which contains all the spectra obtained over the six semesters of our ESO Large program (PI S.C. Trager). This release supersedes our first data release from 2014, with a larger number of spectra (813 observations of 666 stars) and with a more extended wavelength coverage as the data from the near-infrared arm of the X-Shooter spectrograph are now included.

The DR2 spectra consist of three segments that were observed simultaneously (UVB, VIS, NIR) and, if combined, cover the range between 300 nm and 2.45 μm at a spectral resolving power close to $R = 10\,000$. The spectra were corrected for instrument transmission and telluric absorption, and they were also corrected for wavelength-dependent flux-losses in 85% of the cases. The final spectra were corrected for radial velocity and are provided in the rest-frame (with wavelengths in air).

On average, synthesized broad-band colors agree with those of the MILES library and of the combined IRTF and Extended IRTF libraries to within $\sim 1\%$. The scatter in these comparisons indicates typical errors on individual colors in the XSL of 2–4 %. The comparison with 2MASS point source photometry shows systematics of up to 5 % in some colors, which we attribute mostly to zero-point or transmission curve errors and a scatter that is consistent with the above uncertainty estimates.

The spectra cover a large range of spectral types and chemical compositions (with an emphasis on the red giant branch), which makes this library an asset when creating stellar population synthesis models or for the validation of near-ultraviolet to near-infrared theoretical stellar spectra across the Hertzsprung-Russell diagram.

This document does not replace the original paper that any users should read: see [Gonneau et al. 2020 \(2020A&A...634A.133G\)](#).

Overview of Observations

The XSL target stars were selected to cover as much of the Hertzsprung–Russell diagram as possible in the allocated time, with a wide range of chemical compositions. Our original sample consists of 679 unique stars. The primary references for the construction of the XSL target list were existing spectral libraries or compilations of stellar parameter measurements. In particular, the XSL sample has a strong overlap with the MILES spectral library (142 stars, Sánchez-Blázquez et al. 2006; Cenarro et al. 2007) and the NGSL library (135 stars, Gregg et al. 2006). We completed the list with objects from the parameter compilation PASTEL (Soubiran et al. 2010, 2016) and from a variety of more specialised catalogs (see Table A.1 of Gonneau et al. 2020 for details and corresponding references).

More than half of the stars in the XSL library are red giants in the broad sense, which includes red supergiants or asymptotic giant branch stars. These stars provide strong (age-dependent) contributions to the near-infrared emission of galaxies (e.g., Lançon et al. 1999; Maraston 2005; Melbourne et al. 2012). The luminous red stars in XSL are located in star clusters, in the field, in the Galactic bulge and in the Magellanic Clouds (Table A.1). A fraction of the asymptotic giant branch stars are carbon stars, whose spectra have been studied in detail by Gonneau et al. (2016,

2017). We obtained repeated observations for a fraction of the XSL stars (~ 20% of our sample), mainly in the cases of luminous cool stars, known or suspected to vary in time.

We gathered the XSL observations in two phases: a pilot program (Prog. IDs 084.B-0869 and 085.B-0751, October 2009 – September 2010) and a Large Program over four semesters (Prog. IDs 189.B-0925 [A/B/C/D], April 2012 – March 2014). Table 1 summarizes some information related to our observations (e.g., period of observations, number of Observing Blocks).

| Period | Run ID | Number of OBs | Beginning | End |
|--------|-----------------|---------------|------------|------------|
| P84 | 084.B-0869(A/B) | 144 | 2009/10/06 | 2011/03/17 |
| P85 | 085.B-0751(A/B) | 114 | 2010/04/28 | 2010/09/27 |
| P89 | 189.B-0925(A) | 144 | 2012/04/01 | 2013/04/30 |
| P90 | 189.B-0925(B) | 104 | 2012/10/11 | 2013/04/13 |
| P91 | 189.B-0925(C) | 117 | 2013/03/30 | 2014/04/15 |
| P92 | 189.B-0925(D) | 123 | 2013/09/17 | 2014/03/16 |

Table 1: Runs informations.

Please note that the break-down of OBs per period actually refers to the original scheduling and some of the observations were actually carried out at later periods (e.g. due to bad weather conditions).

We observed each science target with two slit widths. We first took a spectrum with a narrow slit to achieve the required spectral resolution. The narrow-slit widths for the UVB, VIS and NIR arms of X-Shooter were 0.5", 0.7", 0.6", respectively, leading to nominal resolutions $R = \lambda / \Delta \lambda \sim 9200$, ~ 11000 and ~ 7770 . With the narrow slits, a wavelength-dependent fraction of the stellar flux is lost. The loss-fraction depends on the seeing, but also on the centering of the star in the slit and on the performance of the atmospheric dispersion corrector of the instrument, both of which are not controlled precisely. The most reliable approach to correct these losses is to observe the targets with a wide slit positioned vertically on the sky. That observation can be calibrated into absolute flux when conditions are photometric and then can be used to correct the energy distribution of the narrow-slit observation of the same target. In non-photometric conditions, as tolerated in our observations ("thin cirrus" tolerance of the ESO VLT scheduling), absolute fluxes cannot be guaranteed, but the shape of the energy distribution is properly recovered with this method under the assumption that the cirrus have a flat transmission curve). We took wide-slit spectra for every target immediately after the narrow-slit ones, using a 5" wide-slit.

We performed our observations using the SLIT spectroscopy mode of X-Shooter. In this mode three observing strategies are available: STARE, NODDING, and OFFSET. We used each of them depending on the desired outcome. In STARE mode the star was located at the center of the slit and the sky background was estimated from each side of the stellar signal on the observed frame. We used this mode for the wide-slit observations. The NODDING acquisition mode allows observations of the star at two positions (A and B) along the spectrograph slit. In this way we achieved an improved sky subtraction with a double-pass subtraction. Almost all our narrow-slit observations were taken in NODDING mode. An OFFSET acquisition mode alternates between the star and an empty sky region. We used this mode for 12 observations of very bright stars in the pilot program.

Release Content

The XSL DR2 data are homogeneously reduced and calibrated, and the spectra are made available in three spectral ranges, corresponding to the three arms of the spectrograph: UVB (300–556 nm), VIS (533–1020 nm), and NIR (994–2480 nm). Our data release contains 2 388 spectra of 666 unique stars, at a resolution $R \sim 10\,000$. This corresponds to 791 UVB spectra, 811 VIS spectra and 786 NIR spectra of these stars.

In Figure 1 we plot the distribution of the selected XSL stars in the sky.

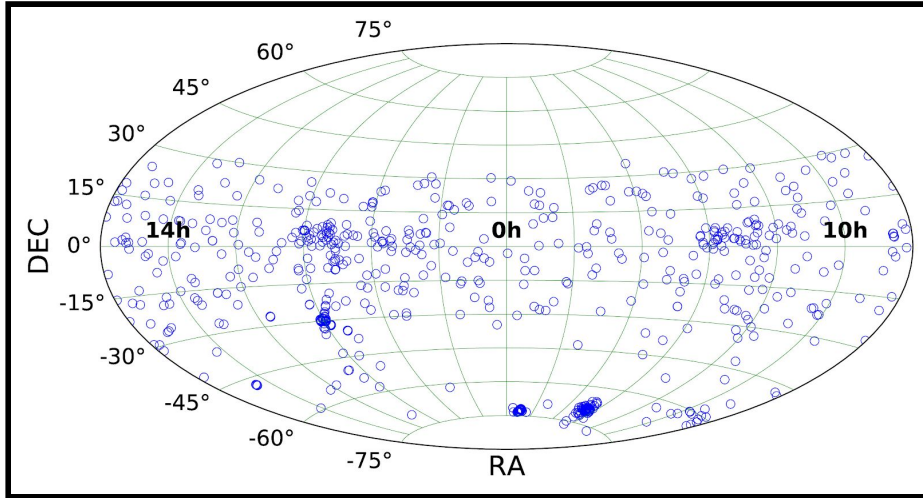


Figure 1: Positions of XSL stars in the sky (Aitoff projection)

Figure 2 presents the stellar atmospheric parameters coverage of the XSL sample as determined by Arentsen et al. (2019) and Gonneau et al. (2017). We refer the reader to Figure 2 of Chen et al. (2014) where the Hertzsprung-Russell (HR) diagram is presented using literature values. Arentsen et al. (2019) estimated atmospheric parameters in a homogeneous manner for 754 XSL spectra of 616 stars: they fit the ultraviolet and visible spectra with the ULYSS package (Koleva et al. 2009) using the MILES spectral interpolator (Sharma et al. 2016) as a reference. Gonneau et al. (2017) determined atmospheric parameters of carbon-rich stars by comparing the observations to a set of high-resolution synthetic carbon star spectra, based on hydrostatic model atmospheres (Aringer et al. 2016)¹.

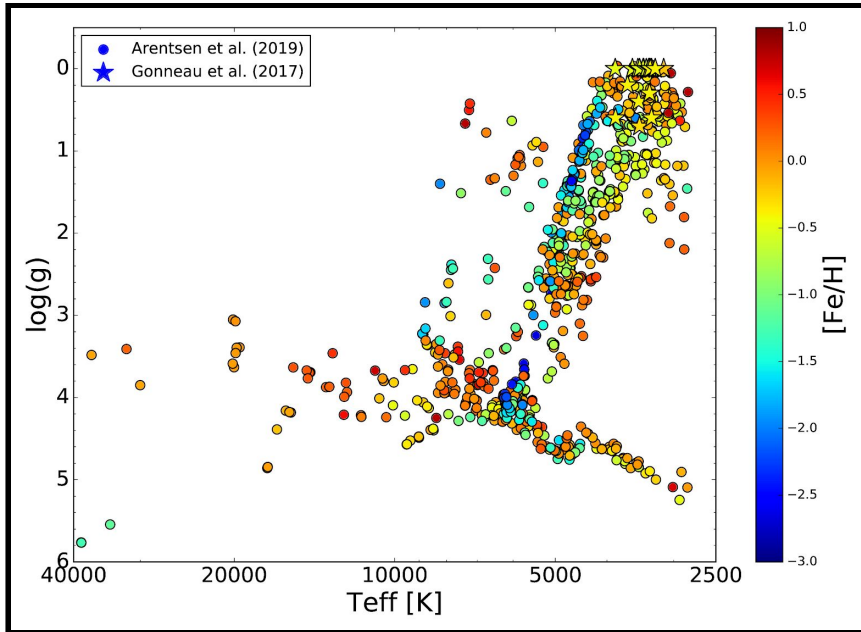


Figure 2: Stellar atmospheric parameters, calculated by Arentsen et al. (2019, open symbols) and Gonneau et al. (2017, star symbols), for 769 XSL spectra.

¹ Only the stars less affected by pulsation (namely stars from Groups A, B and C as defined in Gonneau et al. 2017) are plotted in Fig. 2.

The aim of the selection was to obtain representative spectra mapping the widest area of the parameter space defined by the effective temperature (T_{eff}), the surface gravity ($\log(g)$), and the iron metallicity ($[\text{Fe}/\text{H}]$). Therefore, the sample does not reproduce the natural frequencies of various stellar types. At the time the target lists were prepared, large public catalogs of homogeneous stellar parameter estimates were still lacking, and we were unable to populate certain regions of parameters in a satisfactory way. In particular, some of the Bulge stars selected on the basis of high estimated metallicities turned out to be less metal-rich than expected (Arentsen et al. 2019).

Figure 3 shows the distribution of the spectral types present in XSL, as retrieved from SIMBAD. We highlight the number of stars known as long period variable (LPV) objects in purple. The stars in the 'LPV' bin have no given spectral type but have object types labelling them as LPV objects. The stars in the blue bin 'other' do not have spectral types in SIMBAD, nor have object types which label them as LPV objects.

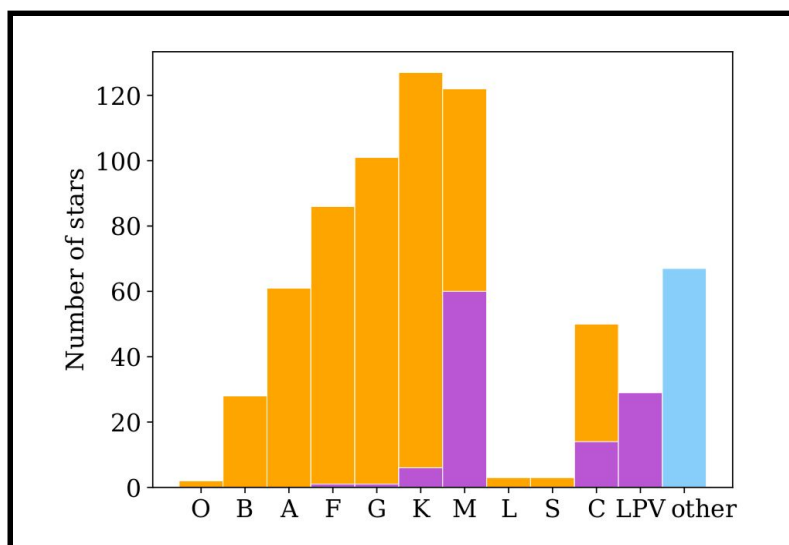


Figure 3: Distribution of the spectral types present in XSL, as retrieved from SIMBAD (figure from Arentsen et al. 2019)

Figure 4 shows the seeing statistics for the XSL DR2 stars.

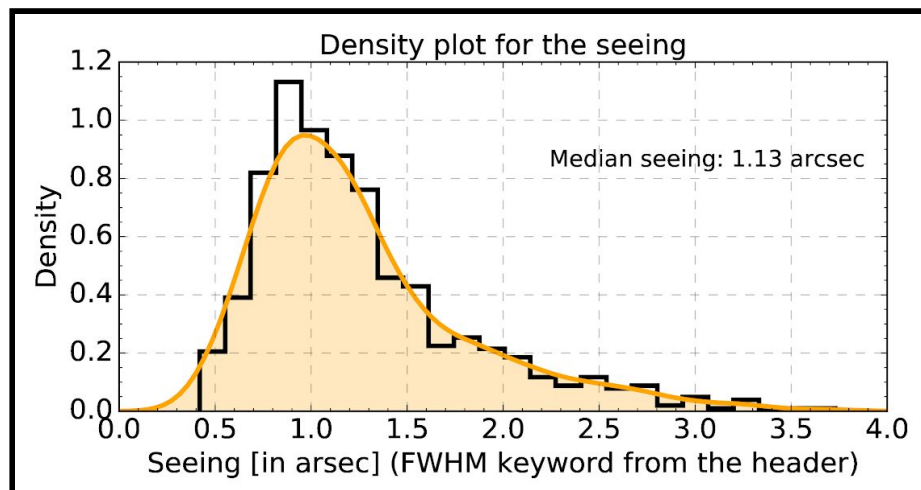


Figure 4: The distribution of the seeing for XSL DR2

Figure 5 shows the distribution of the median signal-to-noise ratios (S/Ns) per pixel for our observations. Except for the coolest stars, typical S/N values are about 70, 90 and 96 for the UVB, VIS and NIR arms respectively. In fact, the S/N for cool stars ($T_{\text{eff}} < 5000$ K) varies drastically with wavelength across the UVB arm. S/N similar to those of warmer stars are found in a temperature-dependent range of wavelength toward the red end of that arm.

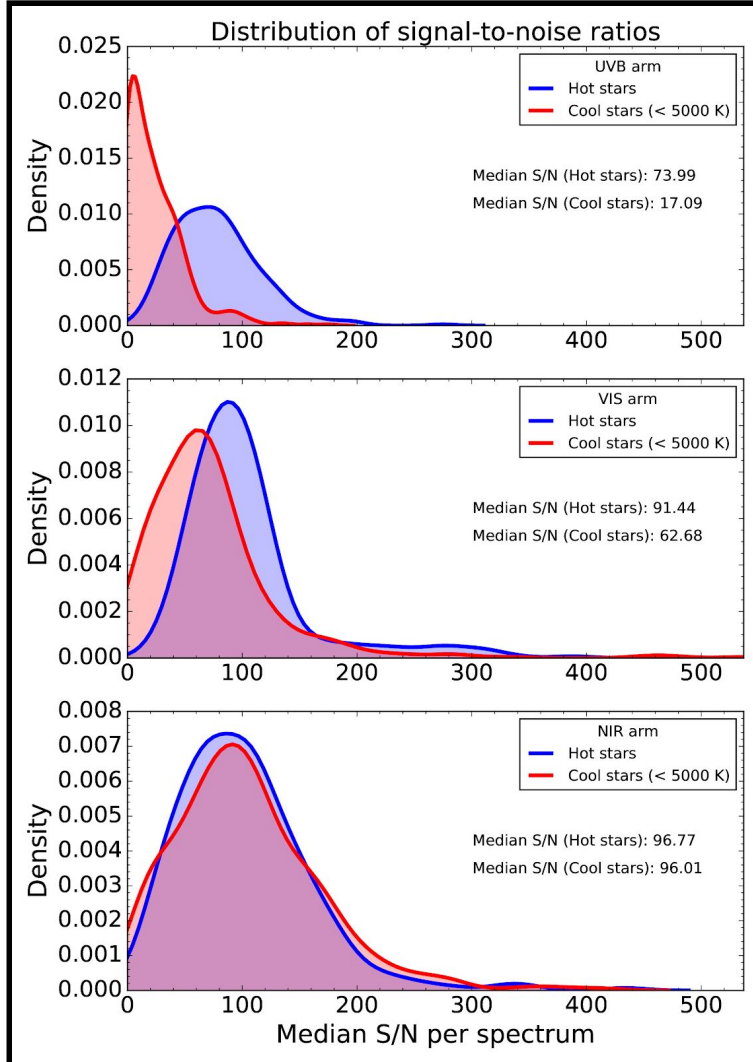


Figure 5: Distribution of the signal-to-noise ratio per arm

The spectral resolution is described by the velocity dispersion measurements of the pPXF fit (Cappellari & Emsellem 2004; Cappellari 2017), as the template spectrum has a much higher resolution ($R \sim 500\,000$, Husser et al. 2013) than the X-Shooter spectra ($R \sim 10\,000$). As the observations span multiple observing periods, the measurements for stars from different observing periods were analyzed separately and then combined. In each observing period, the velocity dispersion results from the pPXF fitting were sigma-clipped with a $5\text{-}\sigma$ threshold. Sigma-clipping was iterated until convergence was achieved. Figure 6 shows the wavelength dependence of the resolution for each observing period and X-Shooter arm. The $1\text{-}\sigma$ error bars belong to period P90 measurements, but are similar for all observing periods. The scatter around the median value comes from stars with lower S/N or a low number of spectral lines in each wavelength region. The red points show the weighted averages of the medians of all observing periods. The resolution is stable throughout the observing periods, with only P84 observations showing slightly lower resolution.

The resolution $R = \lambda / \Delta \lambda$ is also relatively constant with wavelength, although Chen et al. (2014) initially showed otherwise for the UVB arm. However, they only used the F, G, K stars of observing periods P84 and P85. The adopted spectral resolution for each arm is the average value over all wavelengths: 13 ± 1 km/s for UVB, 11 ± 1 km/s for VIS, and 16 ± 1 km/s for NIR. These values are shown with the black dashed lines and the $\pm 1 \sigma$ gray shaded $R = c/\text{FWHM}$ (c being the speed of light). Our adopted values areas in Figure 6 are close to the nominal ones, as can be seen in Table 2. The spectral resolution measures are converted from σ to FWHM assuming Gaussian line profiles in velocity space ($\text{FWHM} = 2.35 \sigma$) and used to re-evaluate the resolving power.

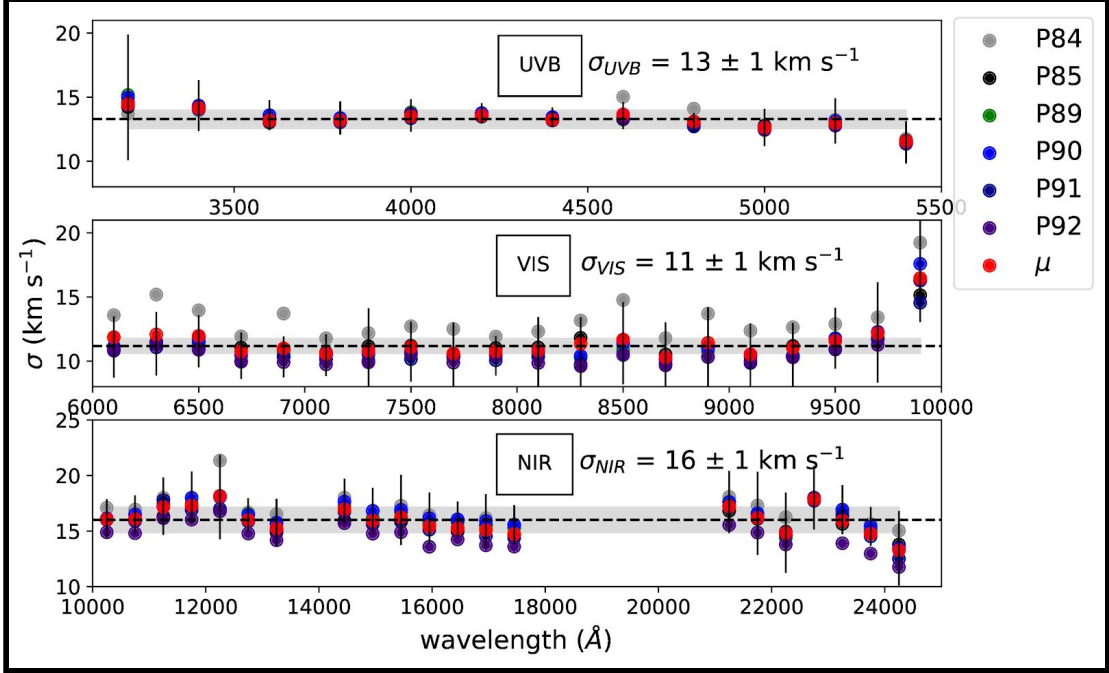


Figure 6: Spectral resolution wavelength dependence for each observing periods. Gray, black, green, blue, dark blue and indigo markers show the medians of measurements of data from observing periods “P84”, “P85”, “P89”, “P90”, “P91” and “P92” respectively. The red point shows the weighted average of all observing periods. The error bars belong to period P90 measurements and are shown for illustrative purposes.

| Arm | σ [km s ⁻¹] | FWHM [km s ⁻¹] | R (our values) | R (nominal values) |
|-----|-----------------------------------|-------------------------------|-------------------|-----------------------|
| UVB | 13 | 30.61 | 9793 | 9700 |
| VIS | 11 | 25.90 | 11573 | 11400 |
| NIR | 16 | 37.68 | 7956 | 8100 |

Table 2: Adopted spectral resolution values per arm

Release Notes

Data Reduction and Calibration

We have reduced the full set of XSL observations over the pilot and the Large Programs in a uniform manner. This allows us to provide an updated calibration of the spectra initially released under DR1 and to ensure a homogeneity of the present DR2. Our data reduction and calibration processes are illustrated in Fig. 7.

We apply the first four steps (referred to as “common data reduction”) to all observations: science target stars and flux standards, wide and narrow slits, and all spectral arms. We use the X-Shooter data reduction pipeline (Modigliani et al. 2010, hereafter XSH pipeline), up to the creation of two-dimensional (2D) order spectra. Then we extract 1-dimensional (1D) spectra outside of the XSH pipeline to better control the rejection of bad pixels. We further apply corrections for the telluric absorption bands and for the continuous atmospheric extinction.

After processing all observations in this uniform way, we derive response curves from the flux-standard spectra, and we use these to process both the narrow and wide slit science spectra. Finally, using the wide-slit spectrum corresponding to each narrow slit observation, we derive a wavelength dependent flux-loss correction and apply it to achieve the final XSL spectrum for each stellar observation.

The final DR2 spectra are then corrected for radial velocity and provided in the rest-frame (with wavelengths in air).

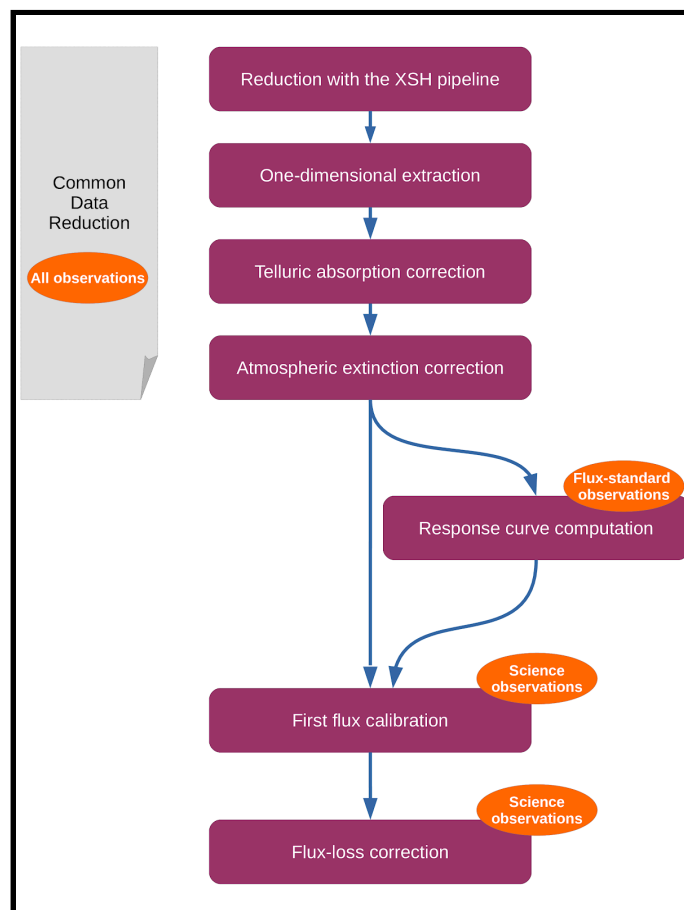


Figure 7: Overview of the XSL data reduction process.

XSH Pipeline

The XSH pipeline consists of a set of data processing modules that perform the individual tasks of the data reduction. These “recipes” can be chained in a flexible way to fulfill the requirement of a specific program. We use the XSH pipeline version 2.6.8, in physical mode as per the pipeline recommendation. In that mode, the wavelength and spatial scale calibrations are performed by optimising a physical model of the instrument. To achieve a more flexible automation of our process we run the XSH pipeline via the Esorex environment (version 3.12). For each science observation, the input to the XSH pipeline is a set of raw data-frames that we identify and collect using the associations of calibration files provided by the ESO archive. When necessary, we modify the default associations to ensure that the flux-standard frames are always reduced with the same flat-field as the corresponding science frames, rather than with the flat-field nearest-in-time. Saturation was a known problem for several observations of the pilot program but occurred rarely in later semesters. Here, we apply a scheme similar to that of DR1 to flag strongly saturated observations automatically and exclude these from further processing.

We used the default parameters for the creation of the calibration frames (up to the *xsh_flexcomp* recipe). To transform the science and flux-standard frames into flat-fielded, rectified and wavelength-calibrated 2D order spectra, we used recipes *xsh_scired_slit_stare* for wide-slit observations, and *xsh_scired_slit_offset* for narrow-slit observations. In particular, we reduced any frames observed in NODDING mode as if they were taken in OFFSET mode, which gives us more flexibility in the handling of bad pixels and improves the quality of our final spectra. In STARE mode, we switch off the sky-subtraction offered by the XSH pipeline because we apply our own algorithm during the subsequent 1D-extraction step. Two key parameters of the above recipes control the sampling of the output spectra along the wavelength axis and along the spatial axis. We set them respectively to 0.015 nm and 0.16 for the UVB and VIS arms, and to 0.06 nm and 0.21 for the NIR arm. The final products of the reduction with the X-Shooter pipeline are 2D frames containing the spectral orders of each arm. They include a map of pixel quality flags and a map of the estimated variances of the pixel errors, which we use to propagate errors through subsequent processing steps.

One-dimensional extraction

A main driver for our choice of performing the extraction of 1D spectra outside of the XSH pipeline was the need for more control over the rejection of bad pixels and the sky subtraction. Our extraction procedure follows a prescription adapted from Horne (1986). It implements a rejection of masked and outlier pixels, as well as a weighting scheme based on a smooth throughput profile, that can follow residual distortions in the rectified 2D-spectra, and on the local pixel-variance as estimated by the earlier steps in the ESO pipeline. The extraction procedure is an updated version of the one presented in Gonneau et al. (2016), and the description below focuses on the modified elements.

Sky background removal

We carried out a sky subtraction for all spectra acquired in STARE mode, as well as for any long-exposure VIS and NIR frames observed in NODDING and OFFSET modes (science frames with exposure times ≥ 600 s in the VIS and exposure time ≥ 200 s in the NIR; flux standard frames with exposure time ≥ 190 s in the VIS and all the NIR frames). The areas along the slit from which the median sky levels are computed are selected in each frame after fitting a Gaussian to the spatial profile of the star, in order to account for the seeing. In STARE mode, these adjustments avoid artifacts such as the negative fluxes that sometimes result from over-subtraction in the standard XSH-pipeline process. In long-exposure spectra, the main purpose is to account for variations in the sky background between the two combined acquisitions.

Updated standard extraction

Horne's extraction scheme relies on obtaining first a rough guess for the 1D spectrum (that we refer to as the standard spectrum) and then optimizing this extraction with an inverse-variance weighted algorithm, that accounts for the spatial profile of the light at a given wavelength (we call the result the final spectrum). To obtain the standard spectrum, we summed the (sky-subtracted) 2D spectrum along the spatial dimension over a limited range of pixels. We updated our procedure by setting the limits to ± 4 or 8 pixels, respectively for NODDING and STARE/OFFSET frames, centered on the peak of the signal. The calculation of the final spectrum is as in Gonneau et al. (2016). Along the spatial axis, the ratio of the flux in a pixel to the normalized spatial profile is taken as an estimate of the stellar flux at the wavelength of interest and these estimates are averaged with an inverse-variance weight. A limited number of iterations are implemented to add outliers to the bad-pixel mask (maximum 3 at any wavelengths), and these pixels are discarded in the final sum.

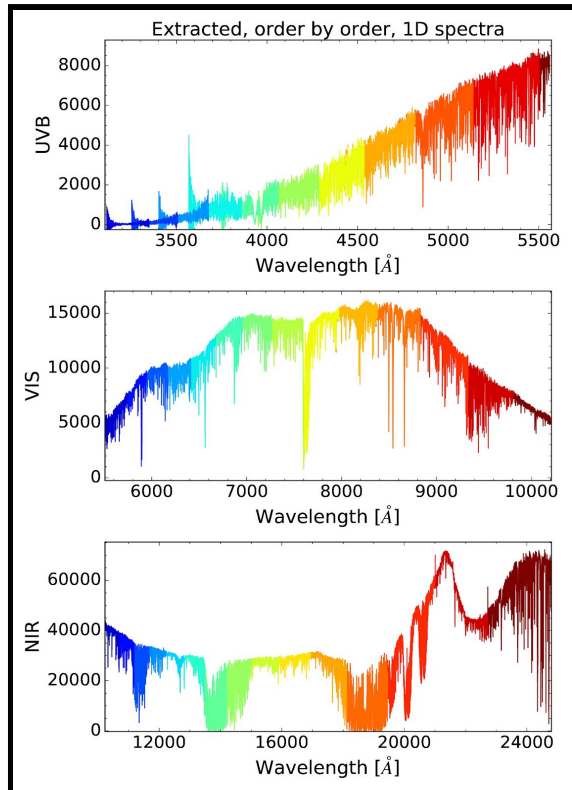
Merging of the individual orders

Figure 8 shows the overlapping orders before merging for each arm of the spectrograph. The flat-fielding algorithm of the XSH pipeline normalizes flat-field frames only globally, hence the blaze function of the instrument is removed in the division by the flat-field, and the extracted orders align well. To merge them, we combined the spectra in the regions of overlap, using weights that combine the inverse variance and a coefficient, α , set to vary linearly from 0 to 1 across those regions. This choice was made because we found that the single-order variance was frequently underestimated at the very end of orders. Hence the flux of each overlapping order, $F_{merging}$, is calculated as follows:

$$F_{merging} = \frac{(1 - \alpha) * F_L/V_L + \alpha * F_R/V_R}{((1 - \alpha)/V_L + \alpha/V_R)}$$

, where F and V stand for pixel fluxes and variances, and subscripts L and R refer to the spectral orders on the left and right sides of region of overlap. For the frames observed in NODDING mode, the 1D extraction procedure produces two separate spectra that we averaged together. The end product of this procedure is a continuous 1D spectrum with two extensions: a flux spectrum and an error spectrum.

Figure 8: Examples of order-by-order spectra for the three arms (XSL observation X0365). From top to bottom: UVB (12 orders), VIS (15 orders) and NIR (16 orders).



Chessboard effect

Some of our NIR frames are affected by an issue that we call the “chessboard effect”. When the seeing is exceptional (typically < 2 pixels per FWHM of the spectral profile in parts of the raw data), the interpolation scheme used by the XSH pipeline for the geometric transformation into a rectified, wavelength calibrated frame does not perform well. The resulting images (known as ORDER2D frames in the pipeline) display a chessboard pattern as illustrated in the top panel of Fig. 9. Because the wavy patterns seen along single lines of the rectified 2D-spectrum vary abruptly between one line and the next, the crests of these waves are mistaken for cosmic ray hits.

To deal with this, we first identify pixels with bit code 6 in the quality-mask images produced by the XSH pipeline (flag 6 = unremoved cosmic rays, cf. the bad pixel code conventions in the X-Shooter Pipeline Manual) and reset these flags to “good pixel”. Then, to avoid any re-flagging by our own extraction procedure, we define a “safe zone” in the 2D frame in which any cosmic-ray identification is switched off. This rectangular zone extends to ± 4 or 6 pixels on either side of the peak of the spatial profile of the spectrum (respectively for NODDING or for STARE/OFFSET frames). This scheme was also used in a few VIS frames. The bottom panels of Fig. 9 show an example of a 2D quality-mask before and after editing, and the extent of the safe zone (represented as a blue rectangle).

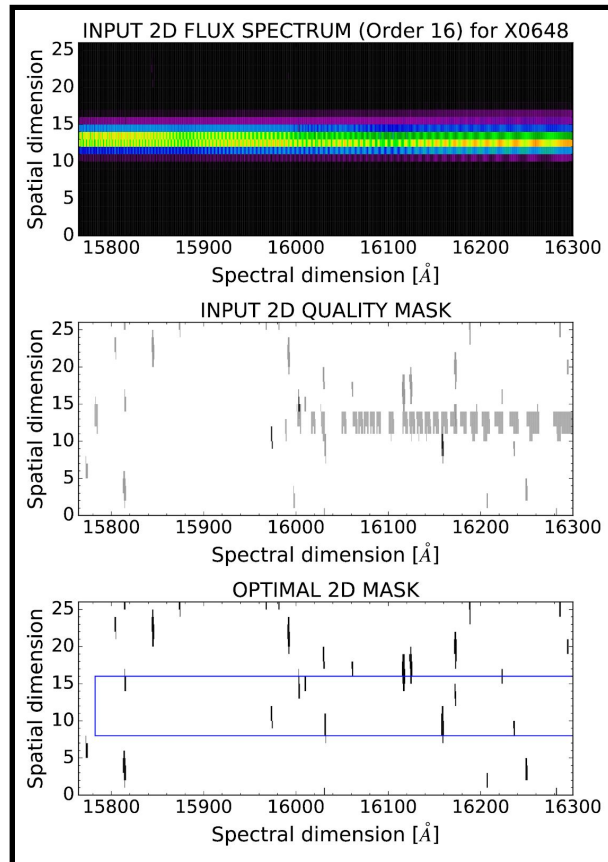


Figure 9: Example of ORDER2D frame affected by the chessboard effect.

Top: Input 2D flux spectrum, before extraction.

Middle: Input 2D quality mask.

Bottom: Optimal 2D mask.

For both 2D masks, the bad pixels are shown in black and gray.

Figure 10 shows a comparison of the different extraction methods, with and without the flagging and the safe zone, for the ORDER 16 of the NIR arm.

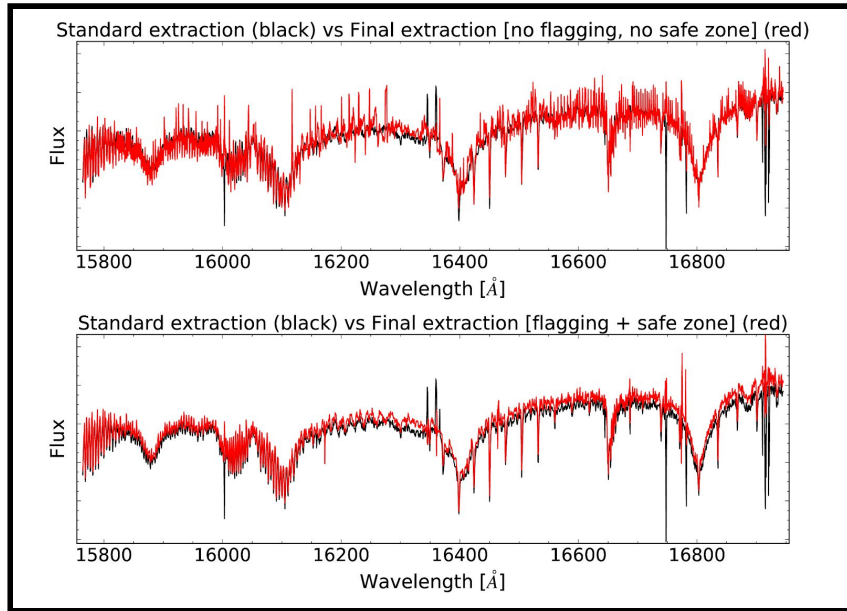


Figure 10: Examples of extracted spectra with the chessboard effect (X0648). The red spectra correspond to the inverse-variance weighted extractions, while the black spectra are for the standard extractions. The original extraction is shown on the upper panel, and the updated extraction to deal with the chessboard effect is shown on the lower panel (flagging and safe zone in the rejection scheme).

Telluric absorption correction

We corrected the 1D extracted spectra for telluric absorption with molecfit (Smette et al. 2015; Kausch et al. 2015). Molecfit uses a radiative transfer code and a molecular line database to calculate a synthetic spectrum of the Earth’s atmosphere based on local weather conditions and standard atmospheric profiles. In addition, molecfit also models the instrumental line spread function. Once the characteristics of the instrument have been taken into account, the synthetic transmission spectrum can be used to correct an observed spectrum for telluric absorption.

Table 1 of Gonneau et al. (2020) details the relevant parameters that we used for running molecfit. Most of these are taken from Kausch et al. (2015), who also applied molecfit to the processing of X-Shooter spectra. In the UVB arm we only corrected for absorption by O_3 , in the VIS arm we corrected for absorption by H_2O , O_2 and O_3 , and in the NIR arm for H_2O , CO_2 , CO , CH_4 and O_2 . Except for water vapor, the abundances of the different molecular species are assumed to be constant and equal to the standard atmospheric values. The total amount of water vapor along the pointing direction of the observation is a free parameter of molecfit that can be fit together with the other free parameters. The wavelength regions used for the fitting procedure are specified in Table 2 of Gonneau et al. (2020). For the NIR arm and the VIS arm, these regions are almost the same as those used in Kausch et al. (2015).

It is known that the wavelength calibration of X-Shooter is not perfect: Moehler (2015) reports shifts with an average peak-to-peak amplitude of 0.28 pixels, corresponding to 0.0042 nm and 0.0168 nm for our VIS and NIR data, respectively. This results in small offsets between the wavelength scale of the spectrum and the synthetic telluric transmission spectrum produced by molecfit. We alleviate this problem by applying molecfit in a slightly different way. First, we use the “classical” molecfit approach, as described in Smette et al. (2015), to derive the precipitable water vapor column (PWV). Then we cut the spectrum into different wavelength segments. The segments are chosen such that each one contains at least one telluric feature and, if possible, also a “clean” region which is (almost) free of telluric contamination. We fix the PWV parameter to the

value found in the first iteration and apply molecfit to each of the wavelength segments. As a final step, the corrected wavelength segments are recombined. Across regions where wavelength segments overlap, we use linearly progressive weights to average the two sets of data.

Our “extended molecfit” approach, where the spectrum of a particular arm is divided into smaller wavelength segments, allows molecfit to find better local wavelength solutions and line spread functions. The final telluric-corrected spectra have a much smaller variance. We use the extended molecfit approach to correct spectra in the VIS and NIR arms. The boundaries of the different wavelength segments are given in Table 3.

| Arm | Wavelength segment [nm] | Arm | Wavelength segment [nm] |
|-----|------------------------------|-----|-------------------------------|
| VIS | $\lambda_{\text{start}}-637$ | NIR | $\lambda_{\text{start}}-1105$ |
| VIS | 633-712 | NIR | 1095-1185 |
| VIS | 708-752 | NIR | 1175-1255 |
| VIS | 748-782 | NIR | 1245-1305 |
| VIS | 778-862 | NIR | 1295-1455 |
| VIS | 858-926 | NIR | 1445-1605 |
| VIS | 922- λ_{end} | NIR | 1595-1755 |
| | | NIR | 1745-1880 |
| | | NIR | 1870-1985 |
| | | NIR | 1975-2040 |
| | | NIR | 2030-2085 |
| | | NIR | 2075-2285 |
| | | NIR | 2275-2385 |
| | | NIR | 2375- λ_{end} |

Table 3: Wavelength segments (air) used for the extended molecfit approach, as described in the text. The extended molecfit approach is only used for the VIS arm and the NIR arm.

Figure 11 compares the two telluric correction approaches: the classical molecfit approach (in gray) and the extended molecfit approach (in red).

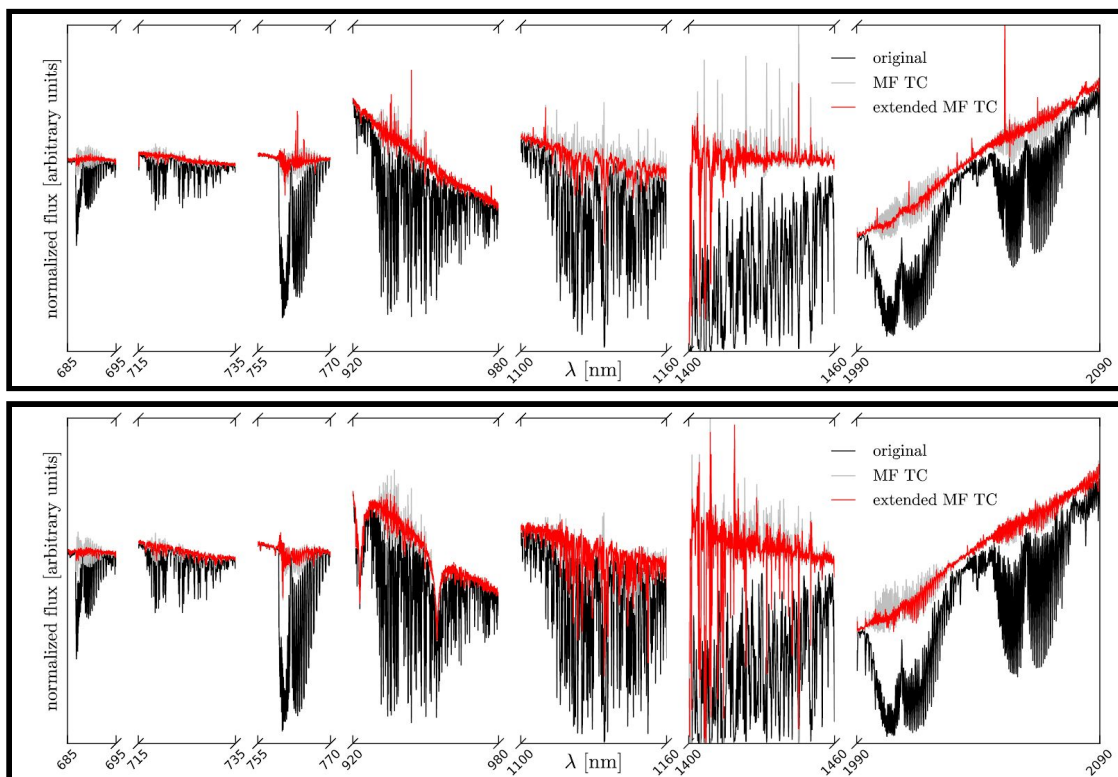
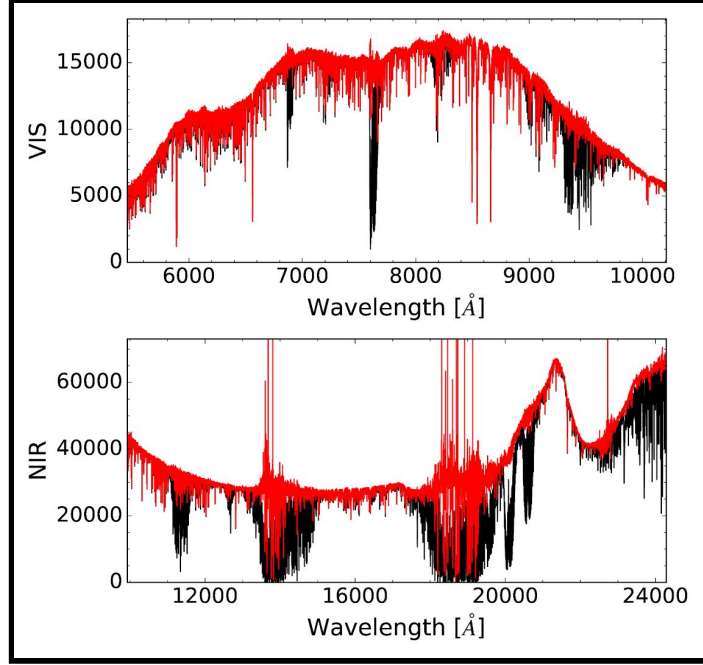


Figure 11: Comparison between telluric correction with the classical molecfit approach (MF TC) and with the extended molecfit approach (extended MF TC). The upper star corresponds to a flux-standard star and the lower star to X0073 (HD 18769). The figure shows different telluric regions in the VIS arm and NIR arm. Within each of these regions, the corrected spectrum is normalized to unit mean.

Figure 12 illustrates the results for the full VIS and NIR wavelength ranges. For the UVB arm, we use the classical molecfit approach since for this arm the wavelength region that contains telluric lines is relatively small.

Figure 12: Before (black) and after (red) the telluric absorption correction process for X0365 (VIS and NIR arms).



Atmospheric extinction correction

Before computing instrument response curves and applying them, the spectra of science and flux-standard stars were corrected for observation-specific effects. We corrected the frames for exposure time, gain and continuous atmospheric extinction as follows:

$$F_{out} = \frac{F_{in}}{exptime \times gain} \times 10^{(0.4 \times airmass \times extinct)}$$

, where F in is the flux of the observations as available after correction for telluric absorption bands. The airmass, exposure time (exptime) and gain were taken from the observation header.

The atmospheric extinction (extinct, expressed in magnitudes per unit airmass) combines aerosol scattering (Mie diffusion, k_{aero}) and Rayleigh scattering (k_{ray}), following Patat et al. (2011). Molecular absorption (including broad features that are sometimes dealt with like a contribution to the extinction continuum) were already accounted for by molecfit. We model the aerosol contribution as advocated by Moehler et al. (2014):

$$k_{aero} = 0.014 \times (\lambda[\mu m])^{-1.38}$$

. The Rayleigh scattering mostly depends on the observation airmass, and only weakly on the atmospheric conditions. In the zenith direction, we model it as:

$$k_{ray} = \frac{p}{1013.25} \times (0.00864 + 6.5 \times 10^{-6} H) \times \lambda^{-(3.916 + 0.074\lambda + 0.050/\lambda)}$$

, with pressure $p = 744$ hPa, height $H = 2.64$ km and wavelength λ in μm (values from Noll et al. 2012).

Figure 13 compares our extinction curve to the XSH pipeline one. From the bottom panel of that figure, we can see that the main differences are in the ozone Huggins bands, which are not deep enough in the reference curve.

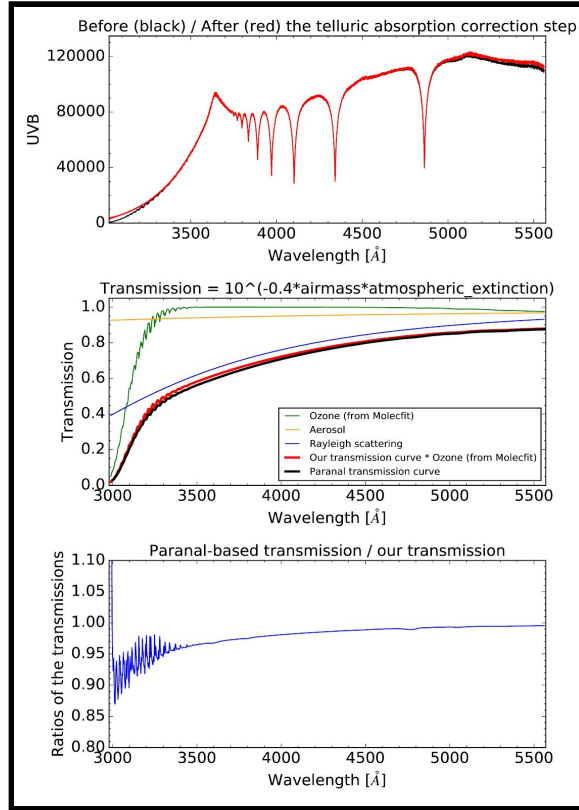


Figure 13: Top: UVB flux-standard spectrum (related to X0365) corrected for O_3 with Molecfit (red spectrum), compared to an uncorrected one (black spectrum). Middle: Our own transmission curve (red curve) – with the details of its three components – compared to the pipeline one (black curve). Bottom: Ratios of the transmissions.

Response curve computation and first flux calibration

To determine a response curve from the 1D spectrum of a flux standard, we performed a χ^2 -minimization between that observation on one hand, and the product of its theoretical spectrum and the unknown response curve on the other. The response curve is represented with a high-order spline polynomial. The typical number of spline nodes is 35 for the UVB and NIR arms and 60 for the VIS. These spline nodes are not all regularly spaced; they are placed sparsely where spurious oscillations should be avoided (e.g., across the telluric water bands in the NIR arm) and more tightly where small-scale instrumental effects must be accounted for (e.g., features at 365 nm due to the combination of two different flat-fields in the UVB arm, the dichroic features at 560-620 nm, a flat-field bump at 2100 nm; see Moehler et al. 2014 for more details). Furthermore, we masked the Balmer lines in the UVB and VIS arms, the O_2 lines in the VIS and the deepest telluric regions in the NIR.

We used the response curves for a first flux-calibration of the science spectra both for the narrow and wide slit observations. The resulting intensities are physical flux densities, in $\text{erg s}^{-1} \text{cm}^{-2} \text{\AA}^{-1}$. These spectra are cleaned from the atmospheric and instrumental effects, except for the slit losses. The narrow-slit spectra, in particular, still do not reflect the absolute distribution of the stellar flux.

Flux-loss correction

For 85% of the spectra, wide-slit observations of sufficient quality are available, and thus the narrow-slit spectra are corrected for wavelength-dependent flux-losses. To this end, we computed a smoothed version of the ratio of the wide-slit over the narrow-slit spectrum, and then fit a low-order polynomial (typically of order 1 for UVB/VIS frames, and 3 for NIR frames). Finally, we multiplied our narrow-slit spectra by this polynomial. In a few cases (3 observations of 2 a priori non-variable stars, namely X0194 [HD 193281] and X0306/X0311 [HD 29391]), when only one of several observations of the same star had an associated wide-slit spectrum or an otherwise more reliable continuum, that observation was used as a reference for the other observation(s).

Rest-frame velocity correction

The DR2 data are corrected for radial velocity and provided in the rest-frame (with wavelengths in air). The barycentric radial velocities, cz , were estimated separately in each of the three arms, because differences between arms are common and often in excess of 10 km s^{-1} (see Moehler 2015, for a discussion). The cz values are available in the header of the final FITS files, together with the barycentric corrections we applied.

In the UVB and VIS arms, the final estimates were obtained with the ULYSS package (Koleva et al. 2009) and the ELODIE 3.2 spectral interpolator (Wu et al. 2011), as also used in the study of stellar parameters of Arentsen et al. (2019). This full-spectrum fitting approach requires an approximate a priori knowledge of the radial velocity for the method to converge, because it performs a local minimization using a Levenberg-Marquardt algorithm. The accuracy of the cz guess should be better than a few times the FWHM of the spectral lines. At the resolution of XSL, the FWHM of the lines is on the order of 30 km s^{-1} , and since the barycentric velocities of the Galactic and LMC/SMC XSL stars are expected to span a range of up to about 400 km s^{-1} , we repeated the fit starting with a series of cz guess in the interval from -300 to $+300 \text{ km s}^{-1}$ with a step of 100 km s^{-1} . For each value of the guess, the atmospheric parameters T_{eff} , $\log(g)$ and $[\text{Fe}/\text{H}]$ as well as cz and the broadening were re-adjusted. The solution with the lowest χ^2 was adopted.

In the NIR, the adopted values of cz were estimated by cross-correlation with the nearest model in the library of synthetic spectra of Husser et al. (2013). Starting from the estimated parameters of Arentsen et al. (2019), we used χ^2 -minimization to identify an adequate near-IR representation of each near-infrared spectrum. The spectral ranges used for the cross-correlation were adjusted based on the effective temperature and spectral type, in order to include a sufficient number of spectral features. In the coolest stars, we avoided regions dominated by a single steep molecular bandhead, as the resulting cz then depend on the way the spectra are renormalized to remove the dominant slope, before the cross-correlation.

For some spectra of cool stars, it was not possible to determine cz in the UVB, or even in the VIS, because of an insufficient flux. When a measurement in the NIR was available, we then simply assigned the latter to the UVB and VIS.

During the preparation of DR2, several methods other than those finally adopted were employed to re-estimate the radial velocities of various data subsets. The distributions of velocity differences between methods typically display an approximately Gaussian peak, with a standard deviation of 2 to 3 km s^{-1} ; non-Gaussian tails of the distributions typically contain $\sim 13\%$, $\sim 18\%$ and $\sim 10\%$ of the stars in the UVB, the VIS and the NIR arms. Hence the value of 2 to 3 km s^{-1} is representative of the uncertainties on the rest-frame wavelengths of the DR2 data.

Data Quality

Quality assurance

After the data reduction, we assigned a number of quality flags to our data based on visual inspection and on experience gained by comparing the observations with synthetic or other empirical spectra (e.g., Gonneau et al. 2017; Lançon et al. 2018; Arentsen et al. 2019). Table 4 (item “Quality flags (per arm)”) describes our flags. The flags were added to the headers of the final FITS files, and peculiarities specific to individual spectra are listed in Table 4 of this document (or Table 8 of Gonneau et al. 2020). We note that this list is not exhaustive, as some artifacts might have been overlooked.

More generic caveats concerning the data are the following. In the UVB, the spectra tend to be wavy near $0.35\mu\text{m}$ (the combination of two different flat-fields D2 and QTH in this range leads to errors) and between $0.545 - 0.55\mu\text{m}$ (known instabilities of the transmission of the dichroic plate that feeds the UVB and VIS arms of X-Shooter).

For the VIS arm, frequent artifacts are seen in the spectral shape between $0.54 - 0.59\mu\text{m}$ (dichroic issue). The continuum at the red end, beyond $0.97\mu\text{m}$, can also have some artifacts (second dichroic region; effect $> 5\%$). Molecfit corrects only for molecular absorption lines, hence telluric absorption by metals is not removed (an example is the frequent contamination of the stellar NaI doublet by telluric Na, between 588 and 592 nm).

In the NIR, a step sometimes arises between the two reddest orders (near $2.25\mu\text{m}$). The noise spectrum does not capture the $1.1\mu\text{m}$ telluric band sufficiently strongly. The slope of the spectrum is sometimes poorly determined below $1.05\mu\text{m}$ (dichroic region; effect $> 5\%$). The K-band is usually of poor quality for hot stars (wavy K-band continuum, lower S/N). Some of these stars are flagged with HAIR_NIR (meaning that there are some narrow spikes in the NIR spectrum, cf Table 4).

| General topic | Step | Keyword ⁽¹⁾ | Description | Default value |
|--|----------------------------------|--|--|---------------|
| General information | | OBJECT | Machine-readable name of the star | |
| | | HNAME | Human-readable name of the star | |
| | | XSL_ID | X-shooter Spectral Library unique identifier | |
| | | XSL_NAME | Internal name for the science spectrum | |
| | | PROV _i | Originating raw science file(s) | |
| Data reduction | ID extraction | EXT_AVG | Two 1D-spectra averaged | F |
| | Response curve | CAL_NAME | Internal name for the response curve used | |
| | | CAL_STAR | Spectro-photometric standard star target | |
| | | CAL_RAW _i | Originating raw flux-standard file(s) | |
| | First flux calibration | FLUX_COR | First flux calibration applied | F |
| Flux-loss correction | LOSS_COR | Correction for slit-losses applied | F | |
| | STA_NAME STA_RAW _i | Internal name for the wide-slit spectrum used Originating raw wide-slit file(s) | | |
| Characterization and quality assurance | Rest-frame correction | REST_COR | Correction to rest-frame applied | F |
| | | REST_VAL | <i>cz</i> value ⁽²⁾ [in km s ⁻¹] | |
| | Barycor values | BARY_COR | Barycentric radial velocity correction value | |
| | Quality flags | SNR | Median signal-to-noise ratio | |
| | WAVY_UVB | WAVY_UVB | Wavy spectrum between 460 and 520 nm (suspected residuals of the blaze function) | F |
| | | WMIN_UVB | Shortest useful wavelength [in nm] | 300 |
| | | HAIR_VIS | Some narrow spikes in the VIS spectrum | F |
| NOIS_VIS | | Noisy VIS spectrum | F | |
| WAVY_VIS | | Wavy in some part of the VIS spectrum | F | |
| WMIN_VIS | WMIN_VIS | Shortest useful wavelength [in nm] | 540 | |
| | HAIR_NIR | Some narrow spikes in the NIR spectrum | F | |
| | WAVY_NIR | Wavy in some part of the NIR spectrum | F | |

Notes to Table 4: (1) The values assigned to the keywords in the headers of the DR2 data files may depend on the arm (UVB, VIS or NIR), even when this is not explicit in the keyword name. (2) The *cz* values are barycentric. They are affected by uncertainties directly related to those on the standard wavelength calibration of the Xshooter data (cf. Sect. 4.3), as illustrated by differences between arms.

Table 4: XSL keywords dictionary (primary header).

Photometric comparison

Chen et al. (2014) compared the DR1 (UVB and VIS) spectra with literature spectra taken from NGSL (Gregg et al. 2006), the calcium-triplet library CaT (Cenarro et al. 2001), and also with higher-resolution spectral libraries such as UVES POP (Bagnulo et al. 2003) and ELODIE (Prugniel & Soubiran 2001). They found a good agreement in the line shapes and depths between XSL and these libraries.

Here we focus on the broad-band spectral energy distribution across the single-arm spectra of DR2. Based on synthetic photometry, we compare colors within the UVB and VIS arms to those of the MILES library (Sánchez-Blázquez et al. 2006); in the near-infrared, we confront the XSL colors with those of the 2MASS survey (Cohen et al. 2003; Skrutskie et al. 2006), and with synthetic colors of the IRTF/E-IRTF spectra (Rayner et al. 2009; Villaume et al. 2017).

Comparison with MILES

Many of the XSL stars were initially selected from the MILES collection (Sánchez-Blázquez et al. 2006). Forty MILES stars were present in XSL DR1, and Chen et al. (2014) found a good agreement between these data in the UVB and VIS arms. In the present release, 173 spectra of 142 stars have a MILES counterpart, of which 164 are corrected for slit-losses. To avoid complications due to the edges of the X-Shooter arms, we define artificial broad-band filters to compare the synthetic photometry of the two data sets (Table 5 and Figure 14).

| Reference set | Filter | $\lambda_{min}[\text{\AA}]$ | $\lambda_{max}[\text{\AA}]$ |
|---------------|--------|-----------------------------|-----------------------------|
| MILES | box1 | 3 900 | 4 500 |
| | box2 | 4 600 | 5 200 |
| | box3 | 5 400 | 6 200 |
| | box4 | 6 300 | 7 100 |

Table 5: Artificial filters used for the MILES comparison.

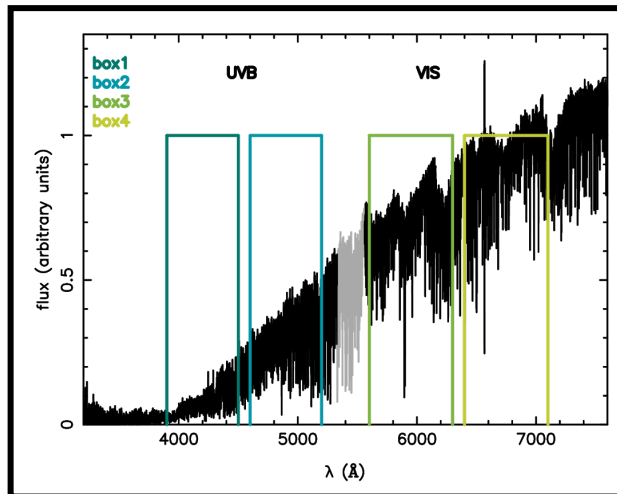


Figure 14: Artificial filters used for the MILES comparison. Filters designed for the comparison with MILES spectra, overlaid on the XSL spectrum of a cool star. The filters avoid the spectral regions most strongly affected by the unstable dichroic between the UVB and VIS arms (plotted in gray).

Figure 15 shows how the MILES and XSL synthetic colors compare. We find excellent agreement in general, with a mean offset of $-0.005/-0.01$ mag and an rms scatter of $0.056/0.032$ mag, respectively for colors $(\text{box1} - \text{box2})$ and $(\text{box3} - \text{box4})$. We have examined outliers with color differences larger than 0.1 mag individually, using plots of the spectra and the extensive comparison of XSL spectra with the theoretical spectra of Husser et al. (2013) that is the subject of another article (in prep.). The clear outlier at the red extreme in the bottom panel is BD+195116B (XSL observation X0440, spectral type M4.0Ve), a flare star. We observed this star at a different phase than MILES. The star is also an outlier in $(\text{box1} - \text{box2})$. Six other outliers at the red end of $(\text{box1} - \text{box2})$ are cluster stars. Five of these are in NGC 6838. We trust their XSL energy distributions to better than 10% because the comparison of these spectra with reddened theoretical models raises no alarms and leads to an extinction estimate that agrees with the values listed in Di Cecco et al. (2015) for the cluster (article in preparation). One object is in NGC 1904, and again best-fit models are not alarming and agree with the very small reddening toward that cluster found in the literature. Still in $(\text{box1} - \text{box2})$, the bluest outlier is a hot star, which is also represented very well with models. Removing those outliers, the rms scatter in $(\text{box1} - \text{box2})$ drops from 0.056 to 0.030 mag. The two outliers in $(\text{box3} - \text{box4})$ not yet discussed are the hot star just mentioned, and an F-type star for which the fit with model spectra excludes large error on the slope in the VIS arm. Removing these, the rms scatter for $(\text{box3} - \text{box4})$ drops from 0.032 to 0.022 mag. Table 6 summarizes these dispersion measurements.

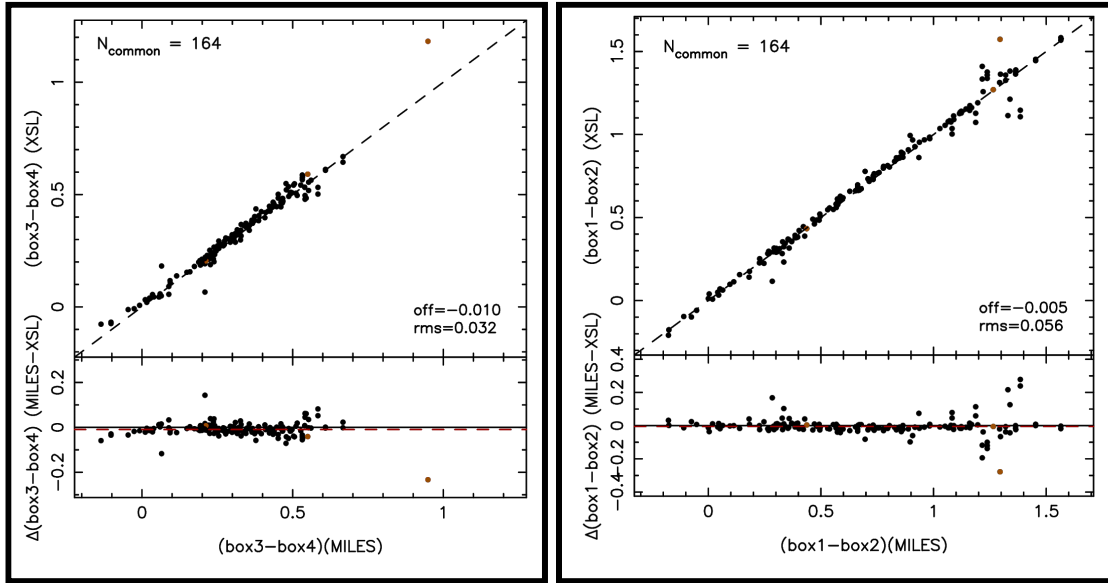


Figure 15: Comparison of synthetic colors between XSL and MILES. Only XSL-spectra with slit-loss corrections are used.

| External reference | Color | Std. dev. σ [mag] | Comments |
|--------------------|-------------------------------|-----------------------------|--------------------------|
| MILES | $(\text{box1} - \text{box2})$ | 0.030 | 0.056 incl. 7 outliers |
| MILES | $(\text{box3} - \text{box4})$ | 0.022 | 0.032 incl. 3 outliers |
| 2MASS | $(J - H)$ | 0.032 | 0.050 incl. 2MASS errors |
| 2MASS | $(H - K_s)$ | 0.038 | 0.056 incl. 2MASS errors |
| IRTF | $(J - H)$ | 0.023 | 0.033 incl. 6 outliers |
| IRTF | $(H - K_s)$ | 0.019 | 0.029 incl. 4 outliers |

Note: The outliers are not the same for all colors. The 2MASS standard deviations listed each include six 4σ outliers. See text for details.

Table 6: Standard deviations of the color-differences between XSL and external datasets

Comparison with 2MASS

The 2MASS filters J, H and K_s fit entirely into the wavelength range of the NIR arm of X-Shooter, as seen in Figure 16. We compute synthetic photometry compatible with 2MASS using the relative spectral response curves and reference fluxes of Cohen et al. (2003). The 2MASS filters J, H and K_s fit entirely into the wavelength range of the NIR arm of X-Shooter, as seen in Figure 16.

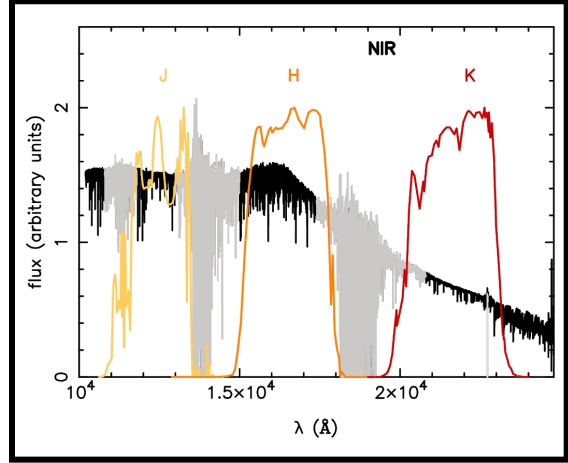


Figure 16: Response curves of the 2MASS filters, overlaid on an XSL spectrum. The transmission curves are taken from Cohen et al. (2003).

Figure 17 shows the results of the comparison. Overall there is good agreement. Small systematic offsets indicate small zero point errors in the exercise; they are in opposite directions for $(J - H)$ and $(H - K_s)$, suggesting a normalization difference in the H band (as also mentioned in Villaume et al. 2017). We find an rms scatter around the mean of 0.050 mag for $(J - H)$ and 0.053 mag for $(H - K_s)$. After removing the contribution explained by 2MASS errors in quadrature, the residual scatter is of 0.032 mag in $(J - H)$ and 0.038 mag in $(H - K_s)$. These are still conservative estimates of the errors in the near-infrared XSL colors, which are clarified in the section “Comparison to IRTF”. In both panels, the larger dispersion toward redder objects is due to cool stars (M and C stars, and stars with $T_{\text{eff}} < 3500\text{K}$), of which many are known or suspected variables.

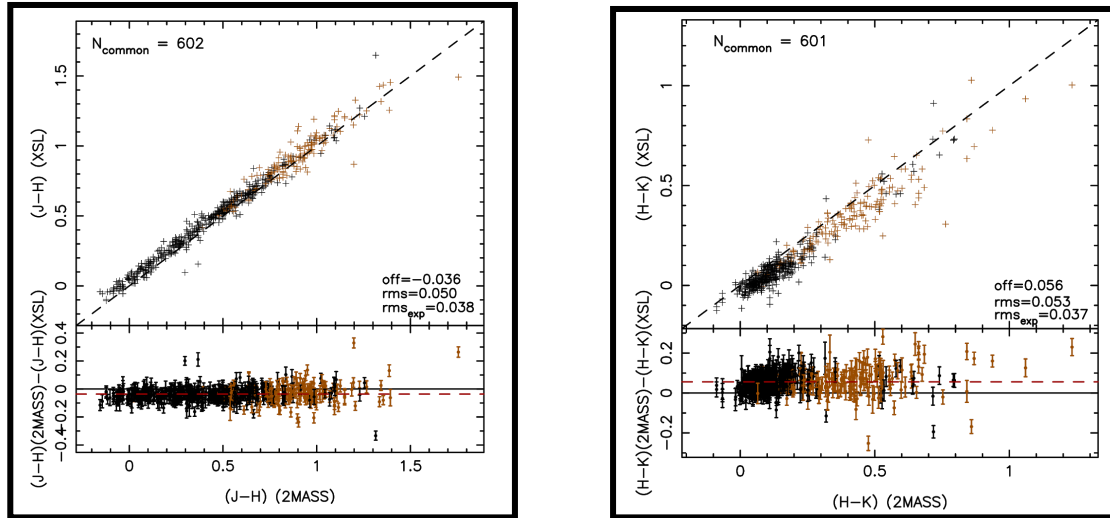


Figure 17: Comparison of synthetic colors between XSL and 2MASS. Only XSL-spectra with slit-loss corrections are used. The brown points correspond to cool stars ($T_{\text{eff}} < 3500\text{K}$ or spectral type M and C). The legends provide the average offset between the colors of the two datasets, the rms scatter around the mean, as well as the part of the rms scatter that is explained by the 2MASS error bars shown in the bottom panels.

Comparison with IRTF

Empirical near-infrared spectral libraries are still rare in the literature. We choose to compare XSL with the IRTF spectral library (Rayner et al. 2009) and its later extension (hereafter E-IRTF, Villaume et al. 2017) as their wavelength range overlaps with ours ($0.7 - 2.5 \mu\text{m}$) and the spectra are flux-calibrated. Their resolution is $R \sim 2000$, and their signal-to-noise ratios are on the order of 100. IRTF contains mainly solar-metallicity stars with spectral types between F and M, plus some AGB stars and L dwarfs. E-IRTF extends the metallicity coverage of IRTF for late-type stars from mainly solar to $-1.7 < [\text{Fe}/\text{H}] < 0.3$. Our sample counts 19 stars in common with IRTF (in practice 25 XSL spectra) and 48 stars in common with E-IRTF (61 XSL spectra), The cross-match between XSL and IRTF then corresponds to 86 spectra in total, and 77 when we restrict the sample to XSL spectra with slit-loss corrections.

Figure 18 shows the comparison. We find a good agreement with insignificant offsets (≤ 0.007 mag) and an initial rms scatter of 0.033 and 0.029 mag, respectively for (J-H) and (H-K_s). We checked all the outliers individually (respectively 6 and 4 cases for these two colors), by overplotting the IRTF and XSL spectra on one hand, and by inspecting the comparison of the XSL spectra with best-fit stellar models on the other. One outlier is a Mira that indeed varied in spectral type between the observations. Another is a star listed as abnormal in Table 7 (X0878). For all other cases, the IRTF SEDs show signs of a discontinuity between the J and the H band, while the comparison between the XSL and the theoretical spectra essentially excludes errors larger than a few percent. Removing the 6 suspicious cases from the sample, the scatter drops to 0.023 mag in (J - H) and 0.019 mag in (H - K_s). Hence a representative value of our internal uncertainties in these near-infrared colors, at least for this subsample, is 2 %.

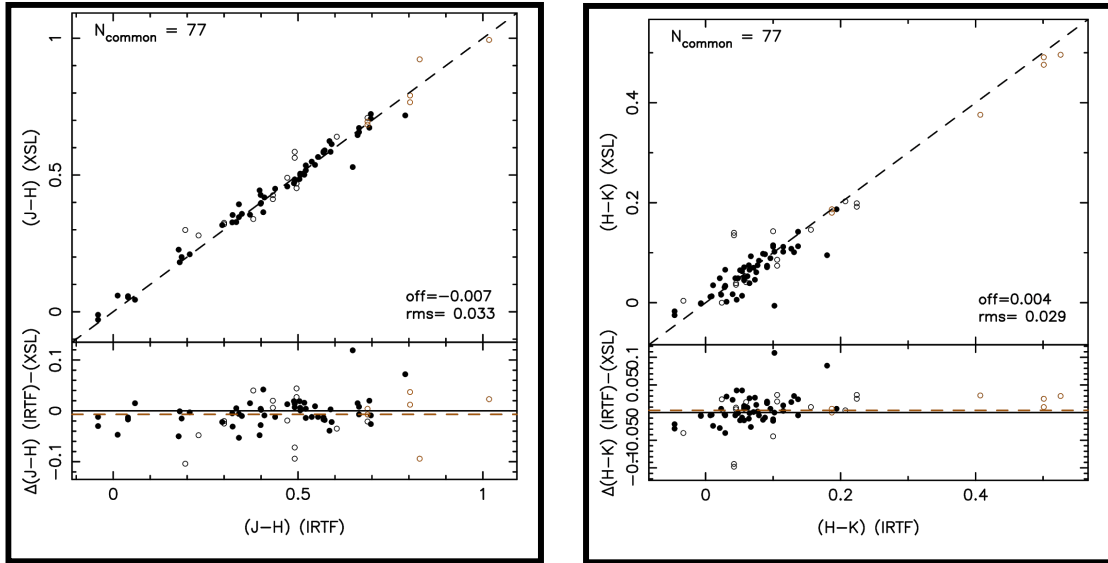


Figure 18: Comparison of synthetic colors between XSL and IRTF (open circles for IRTF and filled circles for E-IRTF). The brown symbols correspond to cool stars (M/C stars, and stars with no spectral type and $T_{\text{eff}} < 3500 \text{ K}$).

Known issues

In this DR2 of XSL, we have chosen to include spectra of peculiar objects that made it into the collection for a variety of reasons, and some spectra with known observational artifacts, because they may be of interest to some future users. We list the most obvious cases in Table B.1 of Gonneau et al. 2020 (or Table 7 of this document). Many of these spectra should not be used in standard population synthesis applications.

| Category | Spectrum (XSL_ID) | Star (HNAME) | Comment |
|--------------------------|----------------------------|---|---|
| Peculiar | X0085, X0133 | HD 96446 | He-rich |
| | X0116 | HD 57060 | P-Cygni emission in H α & He I (1.083 μ m); known eclipsing binary |
| | X0190 | OGLEII DIA BUL-SC19 2332 | O-rich mira, possible TiO emission near 1.25 μ m (Lançon et al. 2018) |
| | X0214, X0248 | HD 190073 | Herbig Ae/Be star, numerous emission lines, continuum contribution from cool component in the NIR arm |
| | X0357 | CD-69 1618 | He-rich |
| | X0420 | SV* HV 11223 | S-star signatures confirmed (ZrO, 940 nm; cf. Wood et al. 1983) |
| | X0424 | CL* NGC 6522 ARP 3213 | Superimposed stars with very different velocities: One dominant in the UVB arm ($v_z \approx -198$ km s $^{-1}$), the other in the NIR ($v_z \approx +30$ km s $^{-1}$). The UVB velocity is used for the barycentric correction in all arms. |
| | X0513 | CL* NGC 4191E 35 | C-star with contamination by nearby hotter star below 450 nm |
| | X0653 | HD 172488 | Possibly He-rich |
| | X0765 | SV* HV 11366 | S-star signatures confirmed (ZrO, 940 nm; cf. Wood et al. 1983) |
| X0798 | SHV 0527122-695006 | M giant with contamination by nearby hot star below 450 nm | |
| Spectral type discussion | X0478, X0675 | V874 Aq1 | O-rich LPV (not C-star as was stated in Nassau & Blanco 1957) |
| | X0587 | IRAS 10151-6008? | O-rich star, (not C-star as assumed in Whitelock et al. 2006). We suspect Whitelock et al. observed 2MASS 10165028-6023549, while we observed 2MASS 10165173-6023466. |
| | X0660 | OGLE 204664e4? | G8V/K0V star. This name was taken from Zoccali et al. (2008), but does not directly relate to the OGLE survey catalogs. Prefer Gaia DR2 4049054206130689024. |
| | X0876 | TU Car | O-rich LPV (as already suggested in Aaronson et al. 1989), not C-star |
| Abnormal | X0061 | SHV 0525478-690944 | C star, NIR poor below 1.3 μ m. |
| | X0085 | HD 96446 | Wavy NIR continuum (prefer X0133) |
| | X0144 | OGLEII DIA BUL-SC26 0532 | A few artificial waves in the VIS arm (residuals from stripes in raw images) |
| | X0196 | HD 194453 | K-band continuum wavy |
| | X0208 | HD 179821 | K-band continuum wavy |
| | X0214 | HD 190073 | K-band continuum wavy (prefer X0248) |
| | X0221 | HD 175640 | K-band continuum wavy |
| | X0237 | SHV 0510004-692755 | A few artificial waves in the VIS arm, as for X0144. |
| | X0269 | HD 163346 | A few artificial waves in the VIS arm, as for X0144. |
| | X0304 | HD 37828 | Continuum poor between 1 and 1.4 μ m (prefer X0097) |
| | X0338 | R Cha | Slightly affected by saturation in the H-band [1600-1700 nm] and K-band [2130-2230 nm] (NIR arm) |
| | X0450 | HD 166991 | Artifacts in K-band (NIR arm) |
| | X0758, X0766, X0790 | Feige 110 | S/N ratio poor in NIR, use average |
| | X0778 | HD 11397 | Artifacts in K-band (NIR arm) |
| X0834 | HD 42143 | Bad telluric correction (O $_2$) in A-band (VIS arm) | |
| X0878 | HD 83632 | Artifacts in H-band (NIR arm) | |
| Deprecated | X0008 | WX Psc | VIS: lack of signal in this wavelength range. |
| | X0020 | ISO-MCMSJ005714.4-730121 | UVB: lack of signal in this wavelength range. |
| | X0029 | ISO-MCMS J005304.7-730409 | UVB: lack of signal in this wavelength range. |
| | X0100 | SHV 0528537-695119 | UVB: lack of signal in this wavelength range. |
| | X0130, X0131 | LHS 2065 | UVB: lack of signal in this wavelength range. |
| | X0154 | BMB 286 | UVB: lack of signal in this wavelength range. |
| | X0253 | OGLEII DIA BUL-SC22 1319 | UVB: lack of signal in this wavelength range. |
| | X0296 | OGLEII DIA BUL-SC13 0324 | UVB: lack of signal in this wavelength range. |
| | X0353, X0605, X0606, X0635 | [ABC89] Cir18 | UVB: lack of signal in this wavelength range. |
| | X0429 | V CrA | UVB: lack of signal in this wavelength range. |
| | X0457 | OGLE-82717 | All three arms: too many different issues and identification uncertain. |
| | X0544 | SHV 0527072-701238 | UVB: lack of signal in this wavelength range. |
| | X0574 | [ABC89] Pup42 | UVB: lack of signal in this wavelength range. |
| X0653 | HD 172488 | UVB: continuum shape unreliable. | |
| X0759 | HV 12149 | UVB: lack of signal in this wavelength range. | |
| X0833 | HD 39970 | All three arms: many issues (including waviness in the UVB, overcorrection of the VIS O $_2$). | |

Table 7: Peculiar stars, abnormal spectra or deprecated objects

Previous Releases

This release supersedes our first data release (DR1) from Chen et al. (2014, A&A, 565, A117). In DR1, we present 246 spectra of 237 unique stars, which were observed during the pilot program, for a wavelength range that was restricted to the two optical arms of X-shooter (300–1024 nm). DR1 was made public on 04/04/14 via our website (http://xsl.astro.unistra.fr/page_dr1.html). The DR1 spectra are also available on the ESO Phase 3 webpages (since October 2020). Those spectra are slightly different than the ones available on the XSL website:

- These DR1 Phase 3 spectra are provided as binary tables with 3 columns and 1 row.
- The headers have been changed to be ESO-compliant.
- The wavelengths are not provided in natural logarithmic spacing (contrary to the XSL DR1 ones), and are provided in nm.

In the current data release (DR2), we present our full set of 813 observations of 666 stars, now also including data from the near-infrared (NIR) arm of X-shooter. We have reduced the full set of XSL observations over the pilot and the Large Programs in a uniform manner. This allows us to provide an updated calibration of the spectra initially released under DR1 and to ensure a homogeneity of the present DR2.

Data Format

Files Types

The XSL DR2 spectra are single-arm spectra, with linearly sampled wavelengths in rest-frame, covering the wavelength range: 300 -- 2 500 nm. The spectra are provided as FITS binary tables, each containing three columns:

1. WAVE: Wavelength [in nm]. As the spectra are rest-framed, the wavelength ranges are spectrum-dependent.
2. FLUX: Flux spectrum [in $\text{erg/s/cm}^2/\text{\AA}$]
3. ERR: Error spectrum: [same units as Flux]

A set of keywords in the headers of the FITS files keep track of various steps of the data-reduction and calibration processes, and of results of the quality assessments. A (non-exhaustive) list of these keywords is given in Table 8 of Gonneau et al. 2020 (or Table 4 of this document).

The DR2 spectra are made available as two separate sets:

1. All the spectra for which a correction for slit-losses across the spectrograph slit was possible (85% of the observations).
2. Remaining 15% of the spectra, without slit-loss correction. They are identified via header keyword LOSS_COR, which is then set to F. Their filenames also contain the *nlc* substring (nlc = not slit-loss corrected).

Acknowledgements

Please cite Gonneau et al. 2020 (2020A&A...634A.133G), when using these data.

Based on data products created from observations collected at the European Organisation for Astronomical Research in the Southern Hemisphere under ESO programme(s) 084.B-0869, 085.B-0751 and 189.B-0925 (PI Trager).

This research has made use of the services of the ESO Science Archive Facility.